Jet ejection following drop impact on micropillared hydrophilic substrates

Anayet Ullah Siddique ®,[1] Marcus Trimble,[1] Feng Zhao,[1] Mark M. Weislogel ®,[2] and Hua Tan ®[1,*]

[1]*School of Engineering and Computer Science, Washington State University-Vancouver, 14204 NE Salmon Creek Avenue, Vancouver, Washington 98686, USA*

[2]*Department of Mechanical & Materials Engineering, Portland State University, 1930 SW 4th Avenue, Portland, Oregon 97201, USA*

Droplet-wall interactions are well known to generate a wide variety of outcomes such as spreading, splashing, receding, jetting, and rebounding. In this paper, we focus on the evolution of jets that form during the recoil of impinging drops on partially wetting hydrophilic substrates composed of cylindrical micropillars. The impact of the millimeter-sized drops of water-glycerol mixtures on the microstructured hydrophilic substrates is investigated by high-speed video photography. Impact velocity and fluid viscosity are varied to characterize the jets. Wetting angles are maintained in the range of $43.6° \leqslant \theta \leqslant 51.4°$. A regime map is constructed to convey the jet behavior at a glance. We find that jet speed, height, and diameter scale linearly with the Weber number. We also find that the jet originates from the inertial collapse of an air cavity formed during the recoil phase of the drop following impact on the microstructured substrate. The relationship between the size of the top jet drop and jet velocity obeys the scaling law of [Gañán-Calvo, Phys. Rev. Lett. **119**, 204502 (2017)] for jets induced by capillary surface singularities. No jet is observed for sufficiently high drop viscosity.

I. INTRODUCTION

Although drop impact dynamics has been studied for more than a century, this ubiquitous phenomenon continues to attract research attention from various disciplines due to its wide range of applications in natural and industrial processes: i.e., ink-jet printing, spray cooling, plasma coating, aerosol formation at ocean surfaces, formation of salt crystals, and others [1–4]. The outcomes of drop impact are incredibly diverse and depend on numerous factors including impact velocity; drop diameter; and fluid, wetting, and substrate properties [5]. In the last two decades, many interesting features of droplet impact have come to light in greater detail with the aid of high-speed video microscopy [3,6,7]. Specifically, jet formation and breakup following droplet impact has received increasing attention [8]. The phenomena is often referred to as Worthington jetting, after A. M. Worthington who first reported it when studying droplet impact on deep water pools [9]. Such jets are commonly observed as a result of pressure waves [8], bursting bubbles [10], and droplet pinch-off [11].

Researchers report that a violent jet is emitted when liquid droplets gently hit a hydrophobic surface at low impact velocity [12–19]. We summarize a selection of reported jetting phenomena in Table I. Nearly all existing studies have reported that jets emerge from drop impact on hydrophobic or superhydrophobic substrates for a certain range of the Weber number (We = $\rho U_i^2 D_i / \sigma$, where ρ, U_i, D_i, and σ are the liquid density, impact velocity, initial droplet diameter, and surface tension, respectively). The jet generation mechanism involves the formation of an air cavity at the center of

---

*Corresponding author: hua.tan@wsu.edu

TABLE I. Summary of studies on jetting phenomenon during droplet impact on solid surfaces.

Reference	Fluid and droplet diameter D (mm)	Solid substrate and contact angle θ (deg)	Findings
Bartolo et al. [12]	Water, $D = 2$	Superhydrophobic, $\theta \sim 160$	Jets shoot out with 40 times the impact velocity at We = 3
Tsai et al. [13]	Water, $D = 2$	Superhydrophobic, $\theta \sim 152$	Jetting for $2 \leqslant$ We $\leqslant 8$
Pearson et al. [14]	Water and water-glycerol mixture, $D = 2.5$	Teflon-coated rib and cavity structures, $\sim 120 \leqslant \theta \leqslant 161$ and $112 \leqslant \theta \leqslant -158$ for water and water-glycerol mixture	For water, high jet in the range of $5 \leqslant$ We $\leqslant 15$, for water-glycerol two-pronged jets in the range of $115 \leqslant$ We $\leqslant 265$
Yamamoto et al. [15]	Water, $2 \leqslant D \leqslant 3$	Stainless steel razor blades with $\theta \sim 82$	For $0.04 \leqslant$ We $\leqslant 5$, the droplet bounced, and for $5 <$ We < 10 the droplet generated a jet
Aria et al. [16]	Water, $D = 2.2$ to $D = 3.8$	Superhydrophobic carbon nanotube arrays, $\theta \sim 171$	Worthington jet occurs in the range of $14 \leqslant$ We $\leqslant 89$
Chen et al. [17]	Water, $D = 2$	Hydrophobic surfaces, $91 \leqslant \theta \leqslant 161$	A high-speed jet arises in the range $3.4 \leqslant$ We $\leqslant 6.1$
Bobinski et al. [18]	Water, $D = 0.6$ and $D = 2.6$	Microstructured hydrophobic surfaces, $150 \leqslant \theta \leqslant 160$	For different microstructures jetting exists in the ranges $41 <$ We < 46 and $42 <$ We < 48
Roy et al. [19]	Water, $D = 2$	Flat Polydimethylsiloxane (PDMS) substrates, $\theta \sim 110$	Jetting and tip breakup at We ~ 6

the spreading drop [15]. The air cavity then collapses during the drop recoil process [15], colliding with itself to generate the pressure spike that forms the jet or geyser [12].

Such jets are also observed when air bubbles burst at the free surface of a liquid [20–24]. Recently, further connections between the jet dynamics and liquid properties have been established [25–27]. As examples, Ghabache et al. [10,25] developed the scaling laws for jet velocity in correspondence with the size of the jet's top drop, initial bubble size, and fluid properties. Gañán-Calvo [28] proposed a set of scaling laws for the jet velocity as well as for the dimensions of the jet as a function of the liquid properties. Deike et al. [21] focused on the velocity of the jet by numerically quantifying gravity's effects on this speed and the conditions under which a top droplet can be ejected from any given jet. It was found that the finite-length jets produced by a bubble burst experience "end pinching," a sequence of droplet detachments from the jet tip, which differ from the Rayleigh-Plateau instability [25]. Gordillo and Gekle [29] examine such end pinching phenomena for jets formed by collapse of the air cavity, which exhibits similar properties to jets formed in myriad scenarios [30,31].

Though much attention has been paid to drop impact on hydrophobic surfaces, less has been directed toward micropatterned hydrophilic surfaces. It is well known that surface morphology plays a significant role in impact phenomena, and with recent developments in micronanofabrication methods, there is rising interest to establish highly structured customized substrates for novel applications relating to self-cleaning surfaces [32,33], lab-on-chip devices [34], and others. Such architectured substrates provide researchers the opportunity to systematically vary substrate morphology to assess drop impact dynamics [35]. The present work aims to investigate jetting following drop impact on microstructured hydrophilic substrates, and to probe the mechanisms underlying such phenomena. We note that such jets are rarely observed from smooth substrate
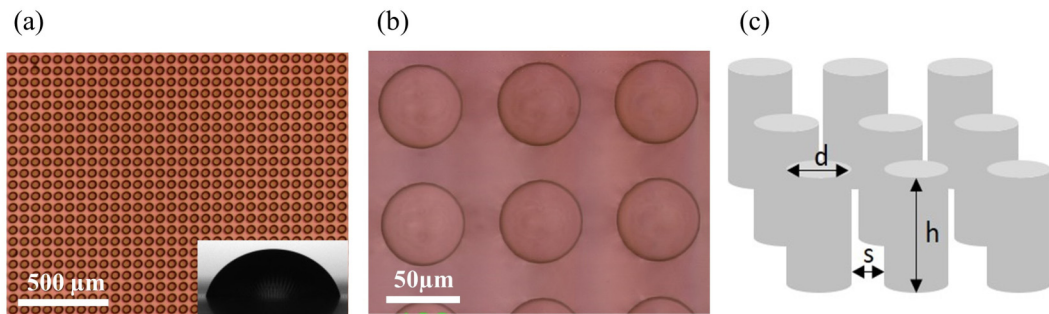
FIG. 1. Microscopic image of micropatterned substrate at (a) 50× magnification—inset shows drop of 55% glycerol solution on substrate with $\theta = 49.4°$ and (b) at 200× magnification. (c) Schematic of microstructure with pillar diameter $d = 52\,\mu$m, height $h = 120\,\mu$m, and spacing $s = 21\,\mu$m.

impact and that we are unaware of such jets reported for impact with partially wetting hydrophilic microstructured substrates in the literature. The silicon substrates used in this study consist of cylindrical micropillar arrays. Water-glycerol mixtures are used to primarily vary liquid viscosity. The impact velocity is varied by adjusting the drop release height. The effects of Weber number and viscosity on the jet formation are quantified via high-speed video photography. The contact angle of different water-glycerol solutions varies from 43.6° to 51.4°.

After a brief description of the materials and experimental setup, a jet regime map is presented and discussed for different impact velocities and viscosities. The jet characteristics including the jet speed, diameter, and maximum height before breakup are then discussed as a function of Weber number. The size and velocity of the top jet droplet due to the breakup of the jet are then quantified and analyzed. We find that the jet is initiated by the inertial collapse of the air cavity formed at the center of the droplet during the recoil stage.

II. MATERIALS AND METHODS

A. Substrates and fluids preparation

In this work we employ micropatterned silicon substrates prepared by metal etch mask patterning via photolithography, metal deposition, lift-off, and dry etch. The common pattern of choice is one of cylindrical pillars of prescribed dimensions. The morphological and structural features of the micropatterned sample are characterized by a Nikon MM-40 microscope via a Nikon DXM 1200 digital camera as displayed in Figs. 1(a) and 1(b). Figure 1(c) provides a schematic of the square lattice micropattern array with measurable pillar geometric parameters: diameter $d = 52\,\mu$m, height $h = 120\,\mu$m, and spacing $s = 21\,\mu$m. De-ionized (DI) water and glycerol (GX0190–EMD Millipore) are mixed with different volume ratios to establish a liquid suite that primarily varies viscosity, as listed in Table II. The Ohnesorge number $\mathrm{Oh} = \mu/(\rho\sigma D_i)^{1/2}$ varies from 0.0023 to 0.028. A Brookfield viscometer is used to measure viscosity. Surface tension and contact angles θ on the substrates are measured using a Model 250 Ramé-Hart instrument with a tensiometer and goniometer. The contact angles for the different water-glycerol solutions are found to vary slightly as listed in Table II for the partially wetting hydrophilic substrates. For the smooth substrate without micropillars, the contact angle for different solutions is nearly constant, 37.4° ± 1.8°.

B. Experimental setup

The experiment consists of a syringe pump, high-speed camera, and precision motion stage as shown in Fig. 2. The microstructured surface is placed on a horizontal stage above which droplets are dispensed from a pipet tip. A programmable New Era Pump Systems NE-1000 syringe pump is

TABLE II. Measured values of density, surface tension, and dynamic viscosity for the various water-glycerol solutions used.

Fluid type (% by volume)	Density $\rho(kg/m^3)$	Surface tension σ (mN/m)	Viscosity μ (mPa s)	Contact angle θ (deg)	Oh
DI Water (W)	997	72	0.96	51.4	0.0023
10% Glycerol (10G)	1027	71	1.3	50.1	0.0029
25% Glycerol (25G)	1070	69.5	2.3	47.1	0.0051
35% Glycerol (35G)	1100	69	3.5	46.4	0.0077
40% Glycerol (40G)	1113	68	4.5	43.9	0.01
45% Glycerol (45G)	1127	67.5	5.8	43.6	0.012
50% Glycerol (50G)	1141	67	7.7	48.5	0.017
55% Glycerol (55G)	1155	66	10.5	49.4	0.023
58% Glycerol (58G)	1162	64	12.8	50.2	0.028

used to deliver the liquid through a syringe to the pipet tip. The diameter of the dispensed drop is maintained at 2.7 mm in all experiments and profile view images of drops captured by the camera are employed to verify this value. Impact velocity is varied from 0.49 to 1.17 m/s by varying drop release height between 120 and 700 mm. A Phantom Miro M310 high-speed camera is positioned horizontally to record the impacting drops in profile. Frame rates between 8000 and 18 000 fps with exposure times of 20 μs are selected. Resulting pixel densities vary between 768 × 768 pixels and 512 × 320 pixels for these choices. The camera employs a Navitar 12x zoom Lens. A high-intensity AmScope LED-8WD spotlight is used for backlighting. Data acquisition and analysis are accomplished via in-house developed MATLAB image processing code (MathWorks Inc.). Before and after each experiment, the micropatterned substrate is washed thoroughly with isopropanol, rinsed with de-ionized water, and dried on a hot plate.
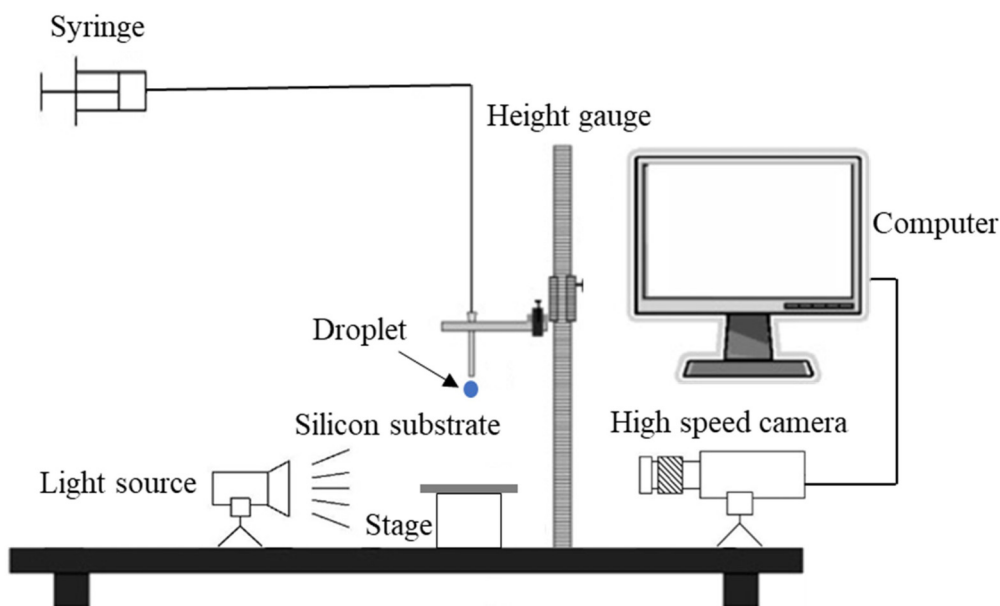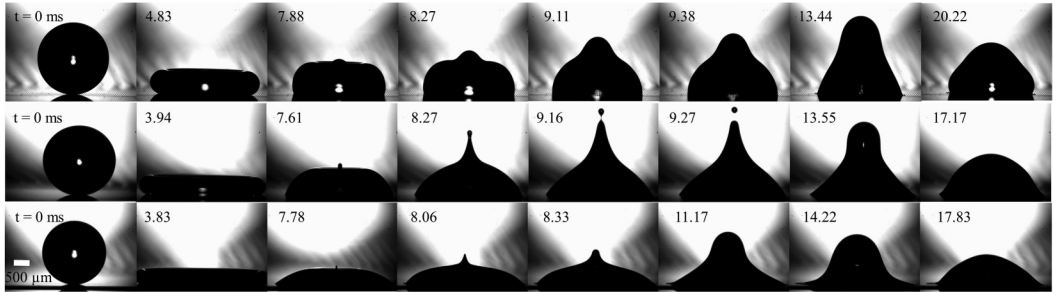

FIG. 2. Schematic of the experimental setup.

FIG. 3. Images of a typical jetting event for 55G fluid between no jet events as a function of impact velocity (We) on the hydrophilic micropillared substrate. Top row: no jet for $U_i = 0.5\,\text{m/s}$ (We = 12); middle row: jet formation and subsequent breakup for $U_i = 0.75\,\text{m/s}$ (We = 27); bottom row: no jet for $U_i = 1.15\,\text{m/s}$ (We = 64).

III. RESULTS AND DISCUSSION

A. Jet formation

When a liquid drop impacts on a solid substrate, its initial spreading is driven by its kinetic energy. After reaching its maximum extent, the kinetic energy of impact is largely converted to liquid surface deflection, and the droplet begins to recoil radially inward due to surface tension forces. On hydrophobic substrates, a thin jet can emerge from the center of the lamella during recoil for a certain range of impact Weber numbers. A similar jetting phenomenon is also found in our experiments for microstructured hydrophilic surfaces. Figure 3 shows the evolution of a drop of viscous liquid (55G, $\mu = 10.5\,\text{mPa\,s}$) impacting the substrate at Weber numbers 12, 27, and 64. It is clear that for We = 27 ($U_i = 0.75\,\text{m/s}$) a jet emerges from the center of the recoiling lamella at 7.61 ms (middle row, Fig. 3). As the jet stretches upward, the tip of the jet grows into a blob until it pinches off to form a satellite droplet that is typically tens of micrometers in diameter. However, no jet is formed from impacts at lower or higher Weber numbers. We note that such jetting phonemenon is not observed for the wafer surface without micropillars. The micropillar structure plays an important role in the jet formation. In our study, if the liquid column emerging from the center breaks up into observable single or multiple so-called jet droplets, we consider the phenomenon as "jetting." Otherwise we consider the impact as a "no jet" event. We find that in all jetting cases the jet begins to appear from the center of the lamella approximately 7.55–7.78 ms after impact. This time corresponds closely with the capillary time scale $(pR_i^3/\sigma)^{1/2} \approx 6.5$ to 6.6 ms [36], a strong indication that jet initialization is governed by inertial-capillary flow.

To understand how impac t velocity and viscosity affect the jet formation, a regime map is constructed in Fig. 4 according to the Weber number We $= \rho U_i^2 D_i/\sigma$ and Ohnesorge number Oh $= \mu/(\rho\sigma D_i)^{1/2}$ for the experiments performed. The values of Oh for the solutions tested are listed in Table II. There are four distinct regimes in the drop impact "jet map" including (1) no jet, (2) jet with a single droplet ejection, (3) jet with multiple droplet ejections, and (4) the partial rebound regime. No jet is observed for viscous damping beyond Oh $\geqslant 0.028$. In such cases the inertial-capillary waves driving the motion to form the jet during recoil are damped in a similar manner as are jets created by viscous bursting bubbles [20]. Further discussion concerning jet formation is reserved for Sec. III D.

For a given liquid, jetting only arises for a range of We in a similar manner to previous studies employing hydrophobic substrates (see Table I). The lower bound of the We range above which the jet appears is higher for our microstructured hydrophilic substrate than those reported in previous studies using hydrophobic surfaces. With further increases in We, the jet generally becomes thinner and shorter for the same liquid as shown in Fig. 5. When We exceeds the upper bound, the no jet regime is again observed. The jet experiences only one droplet ejection at low We, but multiple
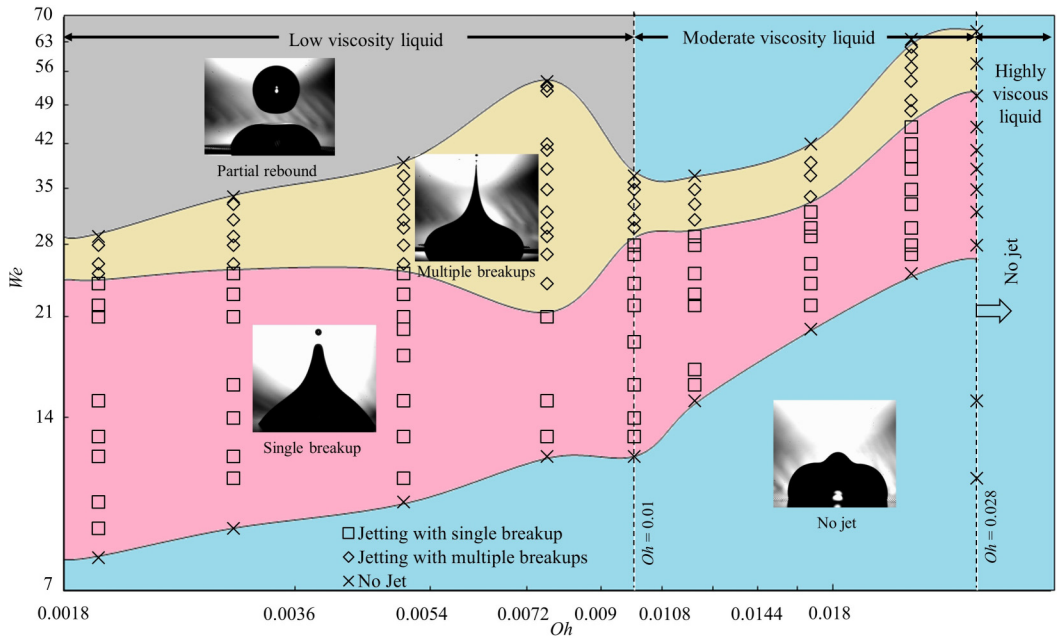
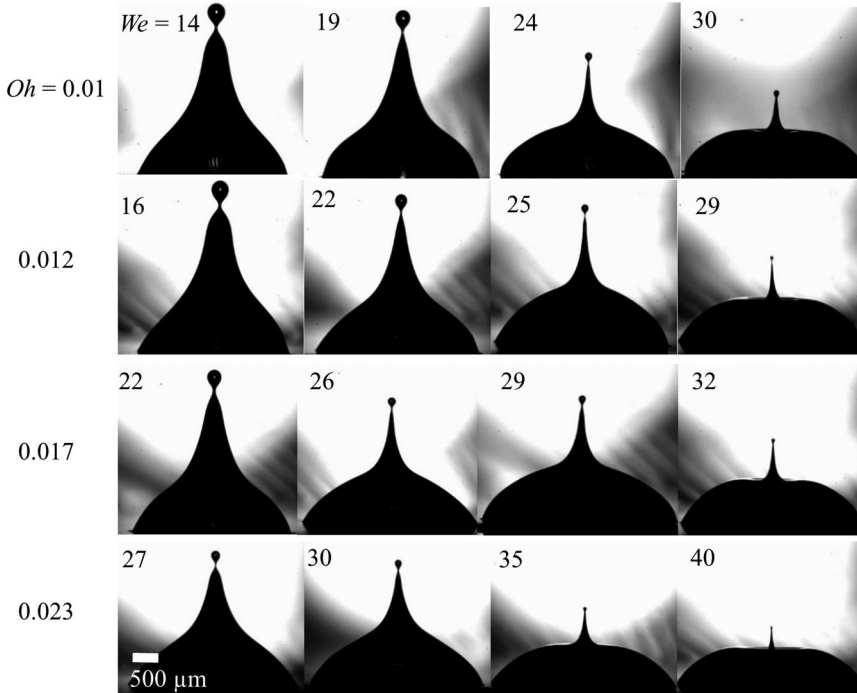FIG. 4. Drop impact jet regime map.

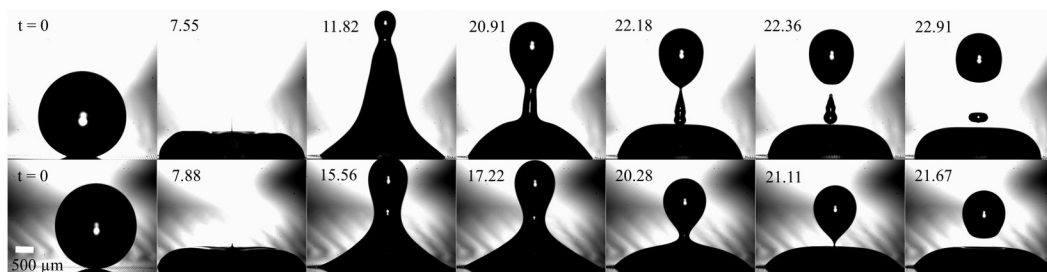FIG. 5. Images of jet after reaching maximum stretch before droplet ejection.

FIG. 6. Partial rebound conditions with elapsed time in milliseconds from initial impact. Top row: impact, jetting, ligament attached to liquid bulb, and liquid-bulb pinch-off for We = 26, Oh = 0.0023. Bottom row: liquid-bulb pinch-off for We = 54, Oh = 0.0077.

droplet ejections at high We, as identified in the two ejection regimes of the map. In both regimes, the lower and upper bounds of the jetting We range increase with increasing viscosity. However, there is an abrupt change in the upper bound of the We range between Oh = 0.0077 (35G) and Oh = 0.01 (40G) solutions.

For water, the transition from single to multiple ejections occurs at We = 25, and the jetting regime is narrow, $25 \leqslant We \leqslant 28$. In this narrow range, after ejection of the jetting droplet(s), inertial and capillary forces continue to drive liquid upward, deforming the droplet into a thick stretched liquid column with a growing bulb on its top that eventually detaches as a large satellite droplet as shown in Fig. 6. Similar behavior is observed during the partial rebound of impacting drops on micropatterned hydrophobic surfaces [19,37]. This type of capillary breakup occurs beyond the upper bound of the jetting regime for water. Herein, such higher-harmonic capillary wave ejections are only observed for the less viscous fluids, Oh < 0.01, and regimes associated with this type of breakup are not addressed in the present analysis which focuses on the initial jet ejection. We also note that drop impact and subsequent jet dynamics for the low-viscosity fluids can vary significantly due to spurious oscillations of the impacting drop induced by the detachment of the drop from the pipet needle. For example, it is noticeable in Fig. 6 that the drop of low-viscosity fluid is not perfectly spherical at the moment of contact with the surface due to such oscillations. Such oscillations alter the spreading and recoiling behaviors and hence the jetting event. Therefore, we confine our study to the jet dynamics of moderately viscous liquids, $0.01 \leqslant Oh \leqslant 0.023$.

B. Jet characteristics

As shown in Fig. 7, V_{jet} is defined as the velocity of the jet tip at the moment it passes the recoiling rim. In some cases, especially for high We, the jet is already fragmented when it emerges above the rim and the top drop velocity is simply approximated as V_{jet}. Jet radius R_{jet} is defined as the half
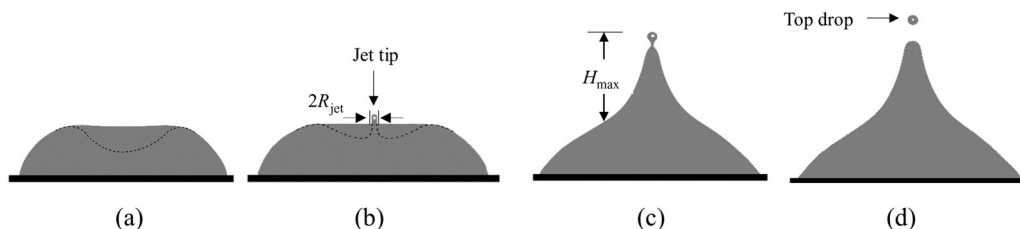

FIG. 7. Schematic of drop shapes following impact. (a) The drop recoils toward the center after maximum spreading (the obscured inside view is identified by the dotted line), (b) the jet rises above the rim, (c) the maximum height of the jet is achieved, and (d) the top drop is ejected.
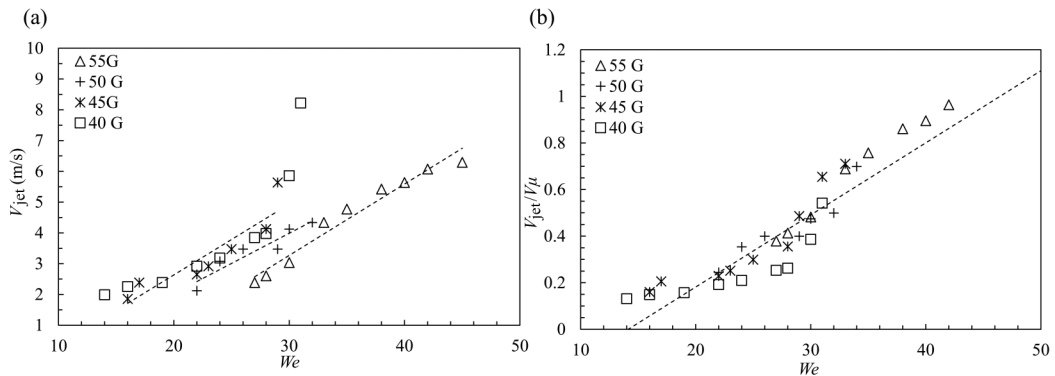
FIG. 8. (a) Jet velocity V_{jet} as a function of We. The dashed lines are linear fits of approximately 1:5. (b) Data in (a) replotted for dimensionless jet velocity V_{jet}/V_μ versus We with linear fit $V_{jet}/V_\mu \sim 0.03$ We.

width of the jet tip when it appears above the rim as shown in Fig. 7(b). The jet maximum height H_{max} is defined as the length of the jet above the rim height before the moment of detachment as shown in Fig. 7(c). To measure H_{max}, the tip of the jet is tracked until the instance of droplet pinch-off.

Figure 8(a) presents the jet velocity V_{jet} as a function of We for the different fluids. At the lower bound of the jetting range, $V_{jet} \approx 2$ m/s for all viscosities. As impact velocity U_i increases, the slow moving thick jet gradually changes into a fast moving thin jet as shown in Fig. 5. For the 40G solution, V_{jet} can reach ∼8.2 m/s. At high We, the rapidly stretching thin jet exhibits multiple breakups and ejects micrometer-sized satellite droplets. For given We, less viscous fluids have higher V_{jet} due to less viscous damping of the capillary wave motion. It is interesting to note that V_{jet} increases nearly linearly with We with approximate slope of 1:5 for the different fluids of Fig. 8(a). We normalize V_{jet} by the viscocapillary velocity scale $V_\mu = \sigma/\mu$. The relationship between V_{jet}/V_μ and We is plotted in Fig. 8(b), where a degree of collapse is observed for $V_{jet}/V_\mu \sim 0.03$ We.

The jet radius R_{jet} and maximum jet height H_{max} for the fluid mixtures are plotted against We in Figs. 9(a) and 9(b), respectively. Both R_{jet} and H_{max} decrease nearly linearly with Weber number as the jet becomes shorter and thinner, i.e., $R_{jet} \sim -0.0062$ We and $H_{max} \sim -0.6$ We. R_{jet} decreases from 140 to 18 μm as We increases from 15 to 40. From Fig. 9(a), the data for R_{jet} versus We fall within a narrow range, suggesting that viscosity plays little role during the early stages of jet formation. Again, we note that H_{max} varies nearly linearly with We with an approximate slope of -3:5.
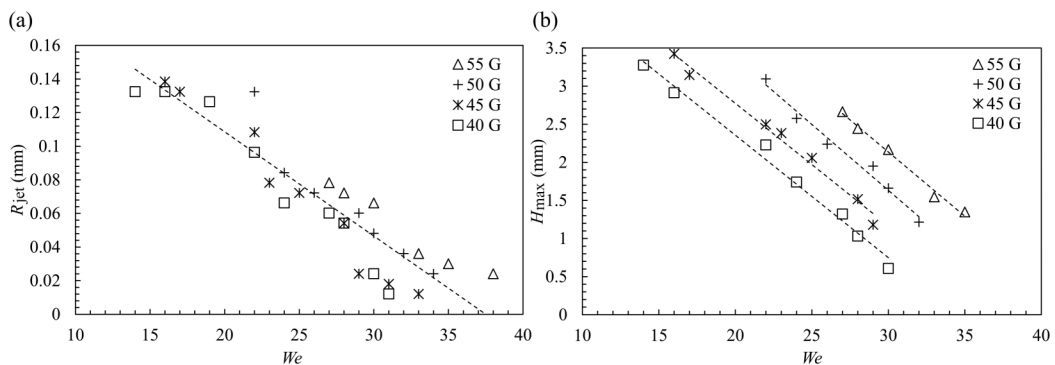

FIG. 9. (a) R_{jet} and (b) H_{max} against We, respectively. Linear fits added for discussion.
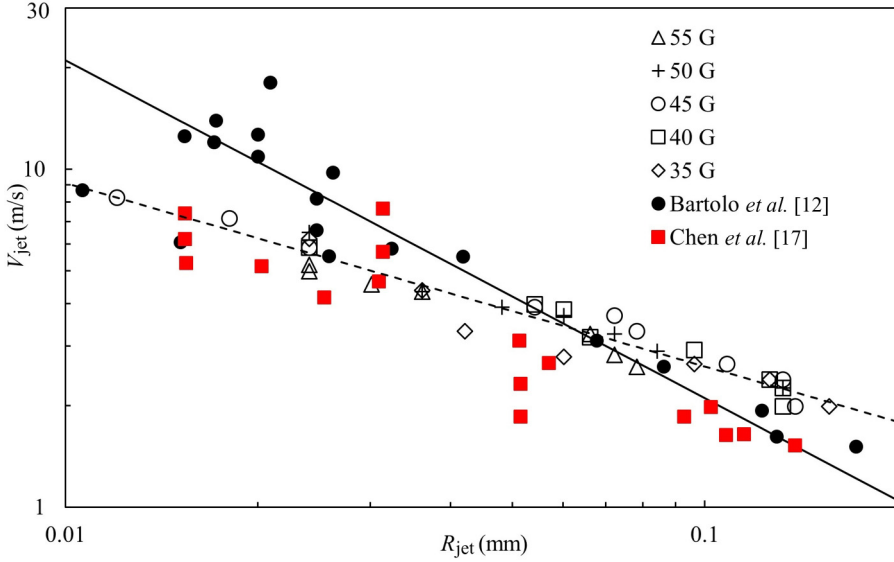
FIG. 10. Log-log plot of V_{jet} against R_{jet} for all liquids tested. Data from Barolo *et al.* [12] and Chen *et al.* [17] involve the jetting induced by the impact of the water droplet of $D = 2$ mm on superhydrophobic surfaces of $\theta \approx 160°$. The dashed line is $V_{jet} \sim R_{jet}^{-0.51}$ fitted from our experimental data. The solid line is $V_{jet} \sim R_{jet}^{-1}$ suggested by Barolo *et al.* [12].

We plot V_{jet} against R_{jet} in Fig. 10, where it is observed how jet velocity decreases with increasing jet radius. The data from Bartolo *et al.* [12] and Chen *et al.* [17] are included in Fig. 10 for comparison. Their experiments involve the impact of a water droplet of diameter $D = 2$ mm on superhydrophobic surfaces with impact velocity varying from 0.3 to 0.6 m/s. Surprisingly, the relationship of V_{jet} versus R_{jet} measured from our experiments follows a similar trend as the experimental results of Bartolo *et al.* and Chen *et al.*, despite the fact that our surface is hydrophilic and very different than those used in their experiments. The reason is that the jetting observed in our experiments is also caused by the same mechanisim, i.e., collapse of the air cavity during the recoiling phase of droplet impact on superhydrophobic surfaces [12–19], which will be discussed in detail in Sec. III D.

Bartolo *et al.* [12] proposed a scaling law $V_{jet} \sim R_{jet}^{-1}$ at the onset of jet formation using the mass and energy balance based on the assumption of jetting induced by collapse of the cylindrical cavity. It is clear from Fig. 10 that unlike the experiment of Bartolo *et al.*, our experimental data do not follow $V_{jet} \sim R_{jet}^{-1}$ closely, which may be due to the fact that the air cavity observed in our experiments (as shown in Fig. 14) does not retain the cylindrical shape all the way until its collapse, a violation of the cavity shape assumption of Bartolo *et al.* However, our data still follow the power law $V_{jet} \sim R_{jet}^{-\alpha}$ with component $\alpha \approx 0.51$ as shown in the dashed line in Fig. 10, which is close to 0.57 obtained by Chen *et al.* [17]. It is noted that despite the range of viscosities (i.e., from 3.5 to 10.5 mPa s) of liquids used in our experiments our data points are collapsed by $V_{jet} \sim R_{jet}^{-0.51}$, which implies that the early-stage formation of the jet is dominated by inertia and capillarity [the Weber number for characterizing the initial jet $We_{jet} = \rho V_{jet}^2 R_{jet}/\sigma \sim O(10)$]. Thus, the inertial-capillary velocity $V_{jet} \sim (\sigma/\rho R_{jet})^{1/2}$ is appropriate for characterizing the relationship between jet velocity and radius, which is in good agreement with $\alpha \approx 0.51$ from our experiments. It is noticeable that the data points of V_{jet} versus R_{jet} for viscous liquids used in our experiments are scattered in a much narrower band than those for water in [12,17], which is due to viscous damping of high-frequency capillary waves excited by droplet impact.
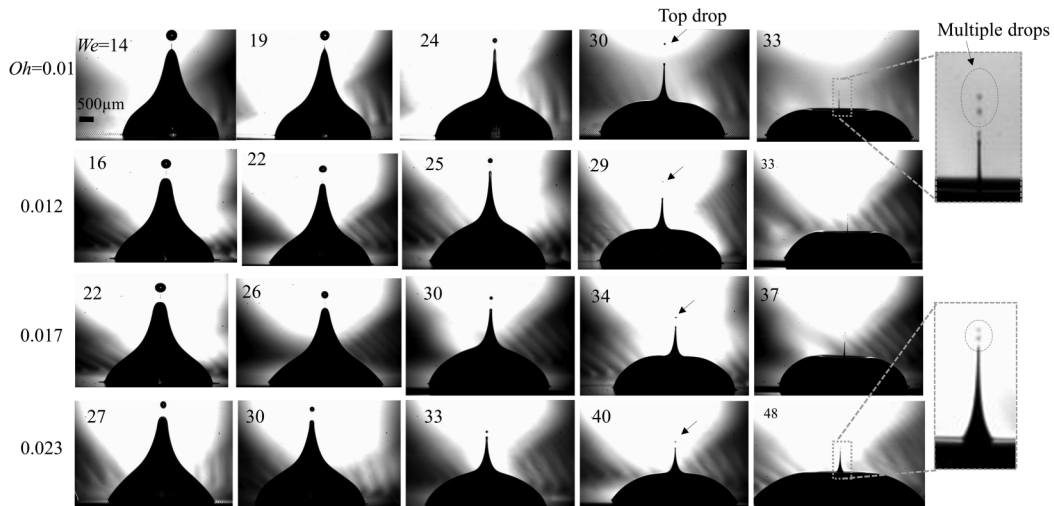
FIG. 11. Images of ejected jet droplets for impacting drops of specified We and Oh. Example of multiple breakups shown in inset at right.

C. Top jet droplet size and velocity

The upward jet in our experiments is stretched inertially with its tip decelerating and pinching off as a consequence of capillary force. The breakup of the jet always takes place at the jet tip detaching one drop at a time, which is similar to the "end pinch-off" phenomena observed in jet droplets produced by bursting bubbles [20–24]. As discussed by Gordillo and Gekle [29], such breakup occurs as a competition between the capillary retraction of the jet tip, the forming of a blob, and a pressure-driven flow from the cylindrical jet toward the bulbous end. A neck develops where the jet joins the blob which eventually ruptures, pinching off one or more satellite droplets. The highly stretched jets in our experiments break up in a way similar to jets observed in bubbles bursting at a liquid surface, the impact of an object on a liquid pool, and inkjet printing [38]. We need to point out that these stretched inertially driven jets do not break as a consequence of the classic Rayleigh-Plateau instability, i.e., growth of capillary waves with wavelengths larger than the jet perimeter resulting in the breakup of cylindrical jets. Instead, the capillary force opposed to the jet tip motion is the major source of perturbations [39].

As the viscocapillary length $l_\mu = \mu^2/(\rho\sigma)$ for our tested liquids is less than 1.5 μm, the breakup of the jet in our experiments is driven by inertia and capillarity [39]. An inviscid breakup typically results in a cone-shaped neck close to rupture as shown in Fig. 5. We have also observed that the liquid-air interface follows a self-similar pattern during the pinch-off process. Thefore, the physics of the pinch-off process is governed by capillary-inertial self-similar dynamics [39]. Figure 11 provides images of top jet droplets for We in the jetting regime. It is clear that for a given fluid the size of the emitted top droplet decreases with the increase in We. For sufficiently high We, the ejected jet droplets become too small to measure with our equipment. No droplets eject when Oh $\geqslant$ 0.028.

The measured diameter of the jet top droplet D_{top} is plotted against the We in Fig. 12(a). For a given fluid, D_{top} decreases as U_i increases as the jet thins. For example, for the 40G solution, the droplet diameter decreases from 469 to 78 μm as We increases from 14 to 30. The size of the emitted top droplets is on the order of micrometers. We find a nearly $-1:4$ linear relationship between D_{top} and We for all liquids tested. We normalize D_{top} by $l_\mu = \mu^2/(\rho\sigma)$ and plot D_{top}/l_μ against We in Fig. 12(b). A collapse is observed for $D_{top}/l_\mu \approx \mathrm{We}^{-\alpha}$ with $\alpha = 3.45$, which confirms that the pinch-off is controlled by inertial and surface tension.
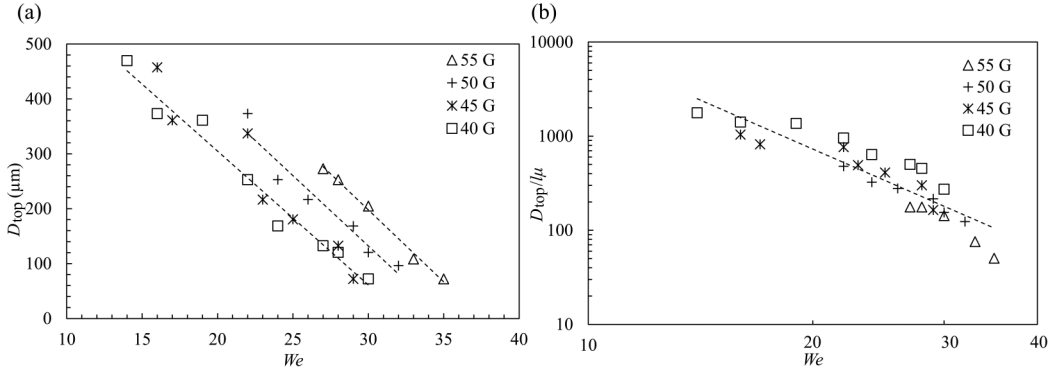
FIG. 12. (a) D_{top} versus We for test fluids. (b) Dimensionless D/l_μ versus We with power fit $D_{top}/l_\mu \approx$ We$^{-3.45}$.

Figure 13(a) presents the velocity V_{top} of the top droplet against We. The droplet velocity increases with increasing impact velocity, which is the same trend as V_{jet} with We. The relationship between V_{top} and We for all fluids is nearly linear with the 1:4 slope. Again employing the capillary velocity $V_\mu = \sigma/\mu$, we define V_{top}/V_μ and plot against We in Fig. 13(b). A suggestive collapse is observed. At the lower bound of the jetting regime, the top droplet for each liquid moves at a speed approximately 0.5–1.2 times that of U_i. However, at the upper bound of the jetting regime, the top droplet moves up to 6 times that of U_i. For extremely thin jets at high We, both size and velocity of the top droplet are difficult to measure due to low resolution and high speed. Thus, no data are presented for high We. For a given We, V_{top} decreases with viscosity.

D. Jet produced by the collapse of the air cavity

It has been reported for drop impact on hydrophobic surfaces that the motion of capillary waves at low We deforms the drop into a pyramidal structure with steps resulting in the formation of a cylindrical air cavity at the center of the drop. The cavity eventually collapses to produce a tiny liquid jet [11–13,15,17]. To see if a similar air cavity is formed for the present micropatterned hydrophilic substrate impact, we conducted several tests with additional lighting from above. Figure 14 provides images of the evolution of a drop impact with We = 30 for the 55G solution. As the drop spreads, the formation of an air cavity at the center of the lamella is clearly observed. The cavity then shrinks
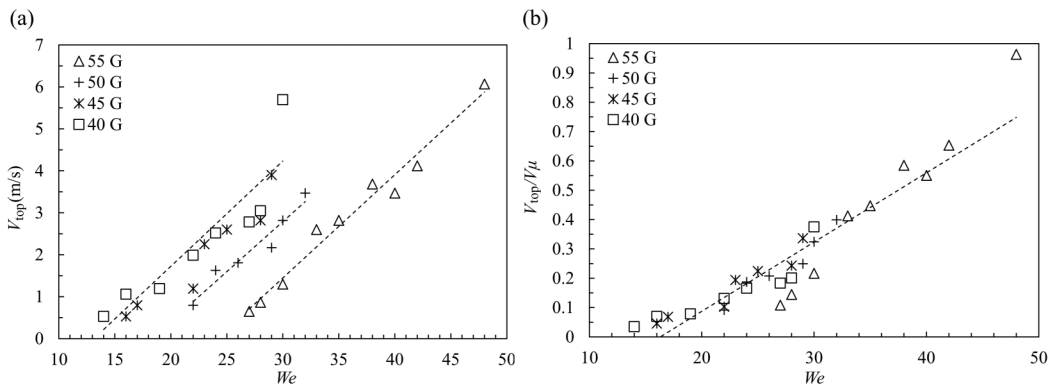

FIG. 13. (a) V_{top} versus We for test fluids. (b) Dimensionless velocity V_{top}/V_μ versus We, with linear fit $V_{top}/V_\mu \approx 0.023$ We.
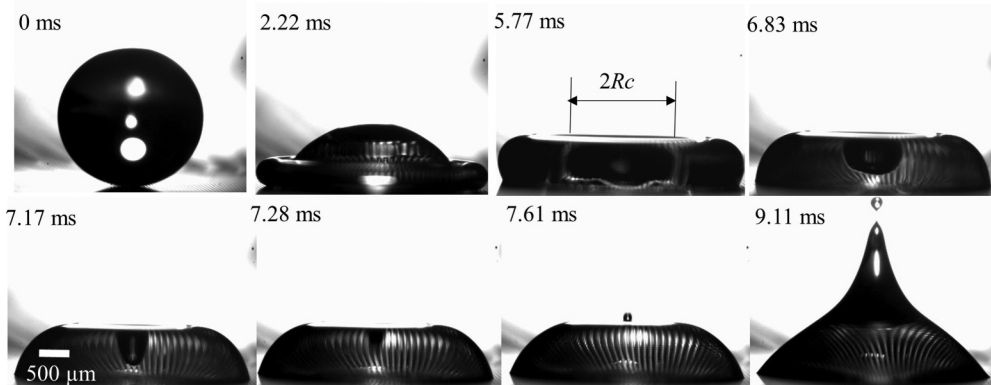
FIG. 14. Image sequence of drop impact of 55G solution at impact velocity of 0.79 m/s, We = 30. An air cavity of diameter $2R_c$ is formed just before 5.77 ms. The air cavity begins collapsing during recoil. Upon collapse, the jet emerges from the center, breaks up, and ejects a 1.30 m/s satellite droplet at 9.11 ms.

during the recoil of the lamella. After collapse of the cavity, a thin liquid jet emerges, elongating until it ruptures, producing a satellite droplet. Due to the relatively high kinetic energy, no pyramid structure of the drop is formed using our microstructured hydrophilic surface, whereas such staircase profiles are often present for hydrophobic or superhydrophobic substrates [11–13,17].

It has been proposed [12,17] that the collapse of the air cavity during drop recoil is governed by the Rayleigh-Plesset equation [40], which describes the collapse of cavitation bubbles. If inertial force dominates the collapse process, it can be shown that the time evolution of the cavity radius R_c follows the power law as $R_c \sim (\sigma R/\rho)^{1/4}(t_c - t)^{1/2}$, where R is the initial drop radius and t_c is the collapse time. Figure 15 plots the measured cavity radius scaled with $(\sigma R/\rho)^{1/4}$ as a function of time for three different liquids used in our experiments. A power-law fit from our data suggests $R_c/(\sigma R/\rho)^{1/4} \approx 1.34(t_c-t)^{0.504}$, the $O(1)$ prefactor supporting the assumption of an inertial collapse mechanism, even for the highest fluid viscosity of these experiments. Our data are also in good agreement with the experimental results from Bartolo et $al.$ [12] and Chen et $al.$ [17] as shown in Fig. 15. If the air cavity collapses through a balance between capillary force and inertia, such as the bursting of air bubbles at the liquid surface, the scaling law for collapse will be $R_c \sim (t_c - t)^{2/3}$ [21,23,41], which clearly does not agree well with our results as shown in Fig. 15. In addition, the evolution of the cavity shape in captured images in Fig. 14 does not show any sign of capillary waves that travel at the liquid-gas interface of the cavity, whereas a typical bursting bubble involves a train of capillary waves propagating and converging at the bottom of the cavity to give rise to the jet. Therefore, the cavity collapse observed in our experiments is driven purely by inertial force, which is different than the capillary-inertial cavity collapse in bubble bursting.

Because the final collapse of the air cavity is indeed a rapid process occurring at micrometer scales [11,12,17], it is not possible for us to observe such limits with our current magnification (12×), resolution (512 × 320 pixels), and frame rate (18 000 fps). As found in other investigations of analogous collapsing surface singularities caused by an inertial focusing mechanism [41], we believe that at the end of the collapse, the inertial flow collides radially producing high pressure at the base of the cavity to deflect the flow in the axial direction to form an axial geyser [29]. We further analyze the relationship between the D_{top} and V_{jet} using the universal scaling arguments of Gañán-Calvo [28]; namely, $D_{\text{top}}/l_\mu \sim (V_{\text{jet}}/V_\mu)^{-5/3}$. Figure 16 plots D_{top}/l_μ versus V_{jet}/V_μ for all of our experimental data in log-log scale. A general collapse of our data points is observed, where $D_{\text{top}}/l_\mu \sim 46.6(V_{\text{jet}}/V_\mu)^{-1.8}$, which we assert is in close agreement with the predictions of Gañán-Calvo, confirming the assumption of inward radial inertial flow colliding into rapid axial motion that inverts the surface curvature at the apex forming the jet. For reference, the line represented
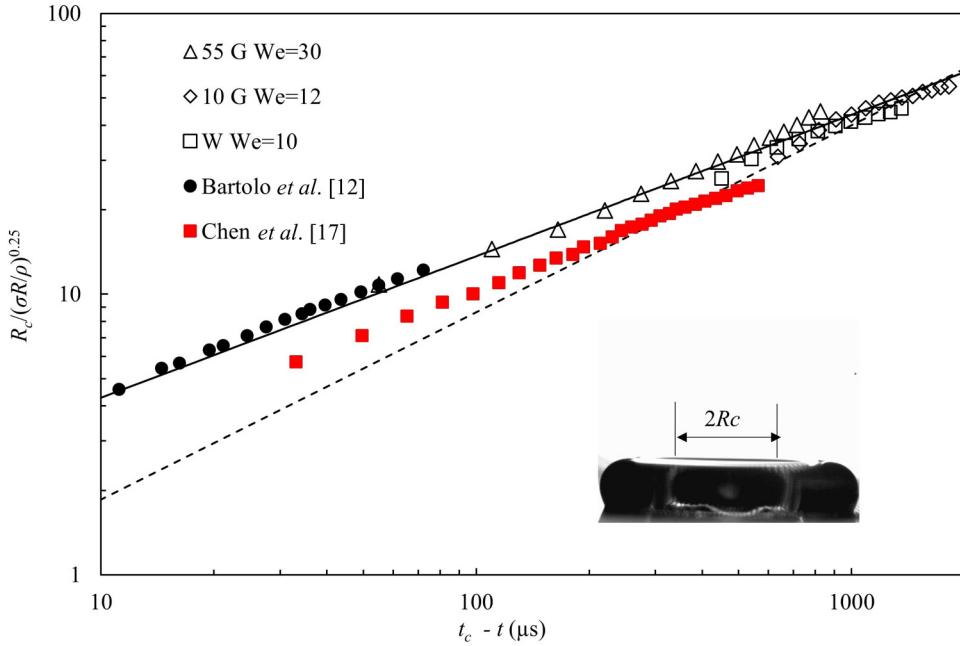
FIG. 15. Log-log plot of dimensionless cavity radius $R_c/(\sigma R/\rho)^{1/4}$ as a function of the time $(t_c–t)$. The solid line is $R_c/(\sigma R/\rho)^{1/4} \approx 1.34(t_c–t)^{0.504}$ fitted from our experimental data. The dashed line corresponds to capillary-inertial collapse with a slope of 2/3. Experiments of Barolo et al. [12] and Chen et al. [17] involve a water droplet of $D = 2$ mm impacting on superhydrophobic surfaces of $\theta \approx 160°$ with We ≈ 7.5.
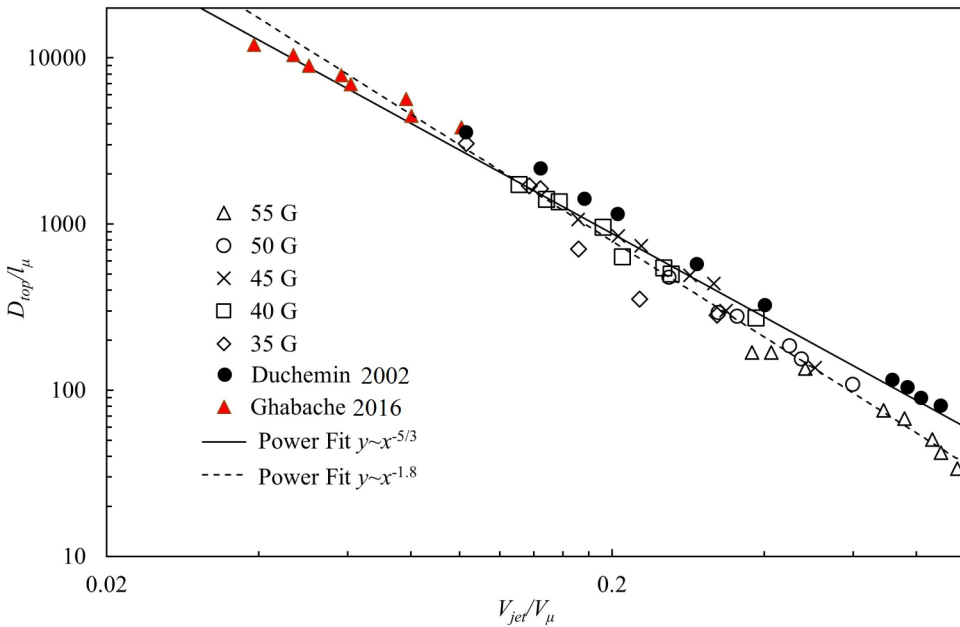

FIG. 16. Dimensionless top droplet diameter D_{top}/l_μ as a function of dimensionless jet velocity V_{jet}/V_μ with two power law fits, $46.6(V_{\text{jet}}/V_\mu)^{-1.8}$ with goodness of fit $R^2 = 0.98$ and $60.0(V_{\text{jet}}/V_\mu)^{-5/3}$ with $R^2 = 0.95$ for our tested liquids. Data of the jetting of bubble bursting in water from Ghabache et al. [42] and Duchemin et al. [43] are included for comparison.

by $D_{\text{top}}/l_\mu \sim (V_{\text{jet}}/V_\mu)^{-5/3}$ is plotted in Fig. 16 as well. The experimental data of Ghabache *et al.* [42] and the simulation results of Duchemin *et al.* [43] for a bubble bursting jet are included in Fig. 16. Despite the fact that jetting in our experiments is caused by pure inertial focusing rather than capillary-inertial focusing, our experimental data of D_{top}/l_μ versus V_{jet}/V_μ follow a trend similar to these from bubble bursting.

IV. CONCLUSION

In this work, magnified high-speed video photography is employed to investigate the ejection of jets from liquid drops impacting partially wetting hydrophilic surfaces consisting of cylindrical micropillars. The drop diameter is maintained at 2.7 mm in the experiments with impact velocities varying between 0.49 and 1.17 m/s. Water-glycerol mixtures are used primarily to vary viscosity between 1 and 12.8 mPa s. We find that the jetting phenomenon arises for certain ranges of Weber (We) and Ohnesorge (Oh) numbers. Within these ranges, the jet ejects one droplet at low We and multiple droplets at high We. The jet regime map constructed conveys the effects of impact velocity and viscosity on the jet dynamics at a glance. As impact velocity increases, the jet becomes thinner and faster. The speed and radius of the jet varies linearly with We. The experimental data show that jet speed depends on jet radius as characterized by the inertial-capillary velocity scale $V_{\text{jet}} \sim (\sigma/\rho R_{\text{jet}})^{1/2}$. The diameter of the top droplet due to the jet breakup is on the order of tens of micrometers. As the impact velocity increases, the top jet droplet also becomes smaller and faster. Again, the top droplet size and velocity vary linearly with We. We find that the jet is produced by the collapse of an air cavity formed at the center of the drop during the recoiling phase of the impact. The transient cavity radius R_c during the collapse is dominated by inertial force and obeys the power-law behavor $R_c \sim (t_c - t)^{1/2}$. Our data reveal that the relationship between the top jet droplet diameter and jet velocity follows the scaling law of Gañán-Calvo [28] for jets created by bursting bubbles, where herein, $\sigma\rho D_{\text{jet}}/\mu^2 \sim (\mu V_{\text{jet}}/\sigma)^{-5/3}$. We in turn suggest that the jets observed in our experiments are generated by pure inertial focusing of radial flow at the point of the air cavity collapse.

ACKNOWLEDGMENTS

[1] M. Rein, Phenomena of liquid drop impact on solid and liquid surfaces, Fluid Dyn. Res. **12**, 61 (1993).

[2] M. Pasandideh-Fard, Y. M. Qiao, S. Chandra, and J. Mostaghimi, Capillary effects during droplet impact on a solid surface, Phys. Fluids **8**, 650 (1996).

[3] A. L. Yarin, Drop impact dynamics: Splashing, spreading, receding, bouncing …, Annu. Rev. Fluid Mech. **38**, 159 (2006).

[4] R. C. A. van der Veen, M. H. W. Hendrix, T. Tran, C. Sun, P. A. Tsai, and D. Lohse, How microstructures affect air film dynamics prior to drop impact, Soft Matter **10**, 3703 (2014).

[5] R. Rioboo, M. Voué, A. Vaillant, and J. De Coninck, Drop impact on porous superhydrophobic polymer surfaces, Langmuir **24**, 14074 (2008).

[6] S. T. Thoroddsen, T. G. Etoh, and K. Takehara, High-speed imaging of drops and bubbles, Annu. Rev. Fluid Mech. **40**, 257 (2008).

[7] C. Josserand and S. T. Thoroddsen, Drop impact on a solid surface, Annu. Rev. Fluid Mech. **48**, 365 (2016).

[8] S. Gekle, J. M. Gordillo, D. van der Meer, and D. Lohse, High-Speed Jet Formation after Solid Object Impact, Phys. Rev. Lett. **102**, 034502 (2009).

 [9] A. M. Worthington, *A Study of Splashes* (Longmans, Green, and Company, London, 1908).

[10] E. Ghabache, A. Antkowiak, C. Josserand, and T. Séon, On the physics of fizziness: How bubble bursting controls droplets ejection, Phys. Fluids **26**, 121701 (2014).

[11] K. Yamamoto, M. Motosuke, and S. Ogata, Initiation of the Worthington jet on the droplet impact, Appl. Phys. Lett. **112**, 093701 (2018).

[12] D Bartolo, C. Josserand, and D. Bonn, Singular Jets and Bubbles in Drop Impact, Phys. Rev. Lett. **96**, 124501 (2006).

[13] P. Tsai, S. Pacheco, C. Pirat, L. Lefferts, and D. Lohse, Drop impact upon micro- and nanostructured superhydrophobic surfaces, Langmuir **25**, 12293 (2009).

[14] J. T. Pearson, D. Maynes, and B. W. Webb, Droplet impact dynamics for two liquids impinging on anisotropic superhydrophobic surfaces, Exp. Fluids **53**, 603 (2012).

[15] K. Yamamoto, H. Takezawa, and S. Ogata, Droplet impact on textured surfaces composed of commercial stainless razor blades, Colloids Surf., A **506**, 363 (2016).

[16] A. I. Aria and M. Gharib, Physicochemical characteristics and droplet impact dynamics of superhydrophobic carbon nanotube arrays, Langmuir **30**, 6780 (2014).

[17] L. Chen, L. Li, Z. Li, and K. Zhang, Submillimeter-sized bubble entrapment and a high-speed jet emission during droplet impact on solid surfaces, Langmuir **33**, 7225 (2017).

[18] T. Bobinski, G. Sobieraj, M. Psarski, G. Celichowski, and J. Rokicki, Droplet bouncing on the surface with micro-structure, Arch Mech. **69**, 177 (2017).

[19] D. Roy, K. Pandey, M. Banik, R. Mukherjee, and S. Basu, Dynamics of droplet impingement on bioinspired surface: Insights into spreading, anomalous stickiness and break-up, Proc. R. Soc. London, Ser. A **475**, 20190260 (2019).

[20] P. L. L. Walls, L. Henaux, and J. C. Bird, Jet drops from bursting bubbles: How gravity and viscosity couple to inhibit droplet production, Phys. Rev. E **92**, 021002(R) (2015).

[21] L. Deike, E. Ghabache, G. Liger-Belair, A. K. Das, S. Zaleski, S. Popinet, and T. Séon, Dynamics of jets produced by bursting bubbles, Phys. Rev. Fluids **3**, 013603 (2018).

[22] R. Mead-Hunter, M. M. Gumulya, A. J. C. King, and B. J. Mullins, Ejection of droplets from a bursting bubble on a free liquid surface—a dimensionless criterion for 'jet' droplets, Langmuir **34**, 6307 (2018).

[23] C.-Y. Lai, J. Eggers, and L. Deike, Bubble Bursting: Universal Cavity and Jet Profiles, Phys. Rev. Lett. **121**, 144501 (2018).

[24] S. Gekle and J. M. Gordillo, Generation and breakup of Worthington jets after cavity collapse. Part 1. Jet formation, J. Fluid Mech. **663**, 293 (2010).

[25] E. Ghabache and T. Séon, Size of the top jet drop produced by bubble bursting, Phys Rev. Fluids **1**, 051901(R) (2016).

[26] G.-J. Michon, C. Josserand, and T. Séon, Jet dynamics post drop impact on a deep pool, Phys. Rev. Fluids **2**, 023601 (2017).

[27] C. F. Brasz, C. T. Bartlett, P. L. L. Walls, E. G. Flynn, Y. E. Yu, and J. C. Bird, Minimum size for the top jet drop from a bursting bubble, Phys. Rev. Fluids **3**, 074001 (2018).

[28] A. M. Gañán-Calvo, Revision of Bubble Bursting: Universal Scaling Laws of Top Jet Drop Size and Speed, Phys. Rev. Lett. **119**, 204502 (2017).

[29] J. M. Gordillo and S. Gekle, Generation and breakup of Worthington jets after cavity collapse. Part 2. Tip breakup of stretched jets, J. Fluid Mech. **663**, 331 (2010).

[30] T. Séon and A. Antkowiak, Large Bubble Rupture Sparks Fast Liquid Jet, Phys. Rev. Lett. **109**, 014501 (2012).

[31] É. Ghabache, T. Séon, and A. Antkowiak, Liquid jet eruption from hollow relaxation, J. Fluid Mech. **761**, 206 (2014).

[32] R. Blossey, Self-cleaning surfaces—virtual realities, Nat. Mater. **2**, 301 (2003).

[33] S. Tamesue, E. Takahashi, S. Kosugi, K. Fukami, T. Mitsumata, N. Tsubokawa, T. Sakka, and T. Yamauchi, Fabrication of a poly(dimethylsiloxane) microstructured surface imprinted from patterned silicon wafer with a self-cleaning property, Polym. J. **48**, 835 (2016).

[34] E. Stratakis, A. Ranella, and C. Fotakis, Biomimetic micro/nanostructured functional surfaces for microfluidic and tissue engineering applications, Biomicrofluidics **5**, 013411 (2011).

[35] H. Tan, Numerical study on splashing of high-speed microdroplet impact on dry microstructured surfaces, Comput. Fluids **154**, 142 (2017).

[36] D. Richard, C. Clanet, and D. Quéré, Contact time of a bouncing drop, Nature **417**, 811 (2002).

[37] D. Kwon, S. Lee, and E. Yeom, Experimental investigation on water repellency and anisotropic wettability of microgrooved polymer surfaces, Exp. Fluids **60**, 169 (2019).

[38] W. van Hoeve, S. Gekle, J. H. Snoeijer, M. Versluis, M. Brenner, and D. Lohse, Breakup of diminutive Rayleigh jets, Phys. Fluids **22**, 122003 (2010).

[39] J. Eggers and E. Villermaux, Physics of liquid jets, Rep. Prog. Phys. **71**, 036601 (2008).

[40] M. S. Plesset and A. Prosperetti, Bubble dynamics and cavitation, Annu. Rev. Fluid Mech. **9**, 145 (1977).

[41] B. W. Zeff, B. Kleber, J. Fineberg, and D. P. Lathrop, Singularity dynamics in curvature collapse and jet eruption on a fluid surface, Nature **403**, 401 (2000).

[42] E. Ghabache, G. Liger-Belair, A. Antkowiak, and T. Séon, Evaporation of droplets in a champagne wine aerosol, Sci. Rep. **6**, 25148 (2016).

[43] L. Duchemin, S. Popinet, C. Josserand, and S. Zaleski, Jet formation in bubbles bursting at a free surface, Phys. Fluids **14**, 3000 (2002).